ACSNANO

www.acsnano.org

ARTICLE

Phase Compatible $NiFe_2O_4$ Coating Tunes Oxygen Redox in Li-Rich Layered Oxide

Jiming Peng,[○] Yu Li,[○] Zhiqiang Chen, Gemeng Liang, Sijiang Hu,* Tengfei Zhou, Fenghua Zheng, Qichang Pan, Hongqiang Wang,* Qingyu Li, Jianwen Liu, and Zaiping Guo*

Cite This: *ACS Nano* 2021, 15, 11607−11618

Read Online

ABSTRACT: Li-rich layered oxides have attracted intense attention for lithium-ion batteries, as provide substantial capacity from transition metal cation redox simultaneous with reversible oxygen-anion redox. However, unregulated irreversible oxygen-anion redox leads to critical issues such as voltage fade and oxygen release. Here, we report a feasible $NiFe_2O_4$ (NFO) surface-coating strategy to turn the nonbonding coordination of surface oxygen into metal−oxygen decoordination. In particular, the surface simplex M−O (M = Ni, Co, Mn from MO_6 octahedra) and N−O (N = Ni, Fe from NO_6 octahedra) bonds are reconstructed in the form of M−O−N bonds. By applying both *in operando* and *ex situ* technologies, we found this heterostructural interface traps surface lattice oxygen, as well as restrains cation migration in Li-rich layered oxide during electrochemical cycling. Therefore, surface lattice oxygen behavior is significantly sustained. More interestingly, we directly observe the surface oxygen redox decouple with cation migration. In addition, the NFO-coating blocks HF produced from electrolyte decomposition, resulting in reducing the dissolution of Mn. With this strategy, higher cycle stability (91.8% at 1 C after 200 cycles) and higher rate capability (109.4 mA g^{-1} at 1 C) were achieved in this work, compared with pristine Li-rich layered oxide. Our work offers potential for designing electrode materials utilizing oxygen redox chemistry.

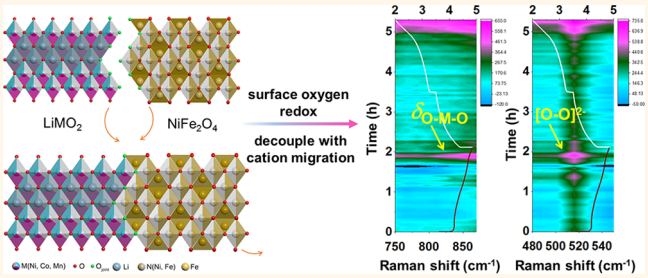

KEYWORDS: *Li-rich layered oxide, lithium-ion batteries, oxygen redox, surface coating, voltage fade*

Nowadays, lithium-ion batteries have become one of the most successful commercial power sources for portable devices and electric vehicles (EVs).[1−3] Despite their energy density approaching 300 Wh kg^{-1}, such a performance is still unable to meet the growing demands for an increased driving range.[4] Li-rich layered oxides, such as $Li_{1+x}M_{1-x}O_2$ ($1 < x \leq 1/3$, M = Ni, Co, Mn), have attracted much attention as they hold the highest energy densities than conventional cathode materials.[5,6] However, these cathode materials suffer from large first-cycle irreversible capacity loss, and voltage/capacity fade during cycling, which seriously limit their practical implementation.[7] These shortcomings are believed to be linked with irreversible anionic redox in the form of O_2 release, which originates from lattice oxygen.[8−11] Nevertheless, previous theoretical and experimental results prove that lattice oxygen in the bulk can experience reversible redox and hence achieve extra reversible capacity.[12−14] Therefore, it is essential to understand the evolution of lattice oxygen in the surface.

Until now, tremendous efforts, including lattice doping,[15−18] surface modification,[19] and particle design,[9,20,21] have been applied to stabilize oxygen redox. Since the irreversible O_2 release and structure collapse initiate at the surface of cathodes,[22−24] surface modification should be effective in this context. Various functional coatings have been applied to limit unwanted oxygen activities and restrict structure degradation. These coatings include metal oxides (Al_2O_3, TiO_2, ZrO_2),[25−27] metal fluorides (LiF, FeF_3, AlF_3),[28−30] phosphate (Li_3PO_4, $AlPO_4$),[31,32] *etc.* The above-reported strategies have shown positive effects on suppressing O_2 release and stabilizing the crystal structure. Besides these coatings, fast lithium-ion conductors ($LiTaO_3$, Li−La−Ti−O, lithium phosphorus oxynitride) were also developed to solve these issues.[33−35] However, these fast lithium-ion conductors are costly for large-scale applications. Therefore, it is of great importance to developing lithium-ion conductors with cost competitiveness.

In the previous work, we have demonstrated a $La_{0.8}Sr_{0.2}MnO_{3-y}$ layer with an $R\bar{3}c$ hexagonal structure

Received: March 8, 2021
Accepted: June 15, 2021
Published: June 24, 2021

https://doi.org/10.1021/acsnano.1c02023
ACS Nano 2021, 15, 11607−11618

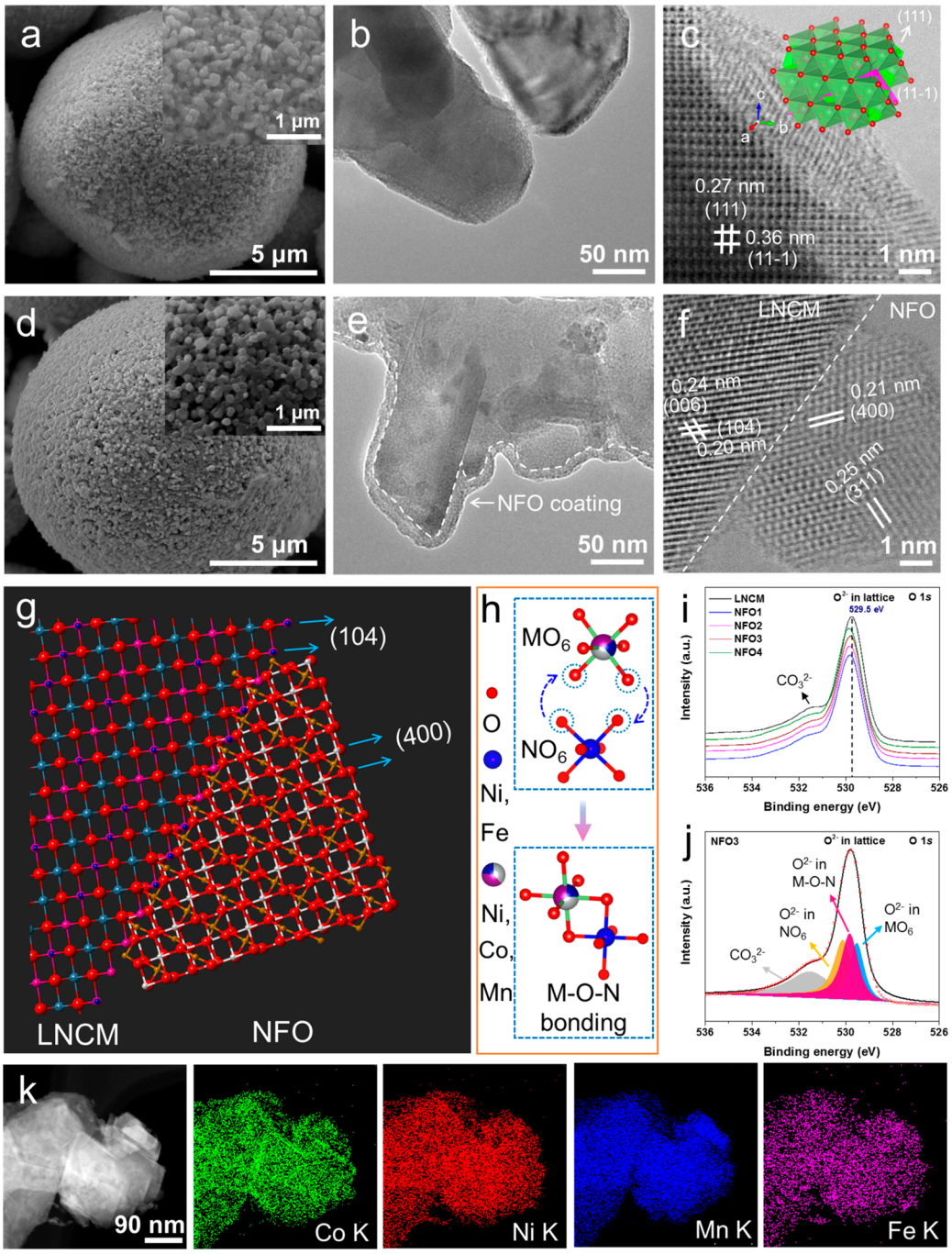

Figure 1. Morphological and structural characterization of pristine LNCM and NFO3. Scanning electron microscopy (SEM), TEM, annular bright-field scanning transmission electron microscopy images of (a−c) pristine LNCM and (d−f) NFO3, respectively. (g) Schematic illustration of LNCM/NFO lateral heterointerface. (h) Schematic of M−O−N bonding. (i) XPS O 1s spectra of pristine LNCM and NFO-coated LNCM samples. (j) XPS O 1s spectra of NFO3. (k) STEM-EDS mapping of NFO3.

symmetry being coated onto Li-rich layered oxide (the main phase having hexagonal $R\bar{3}m$ symmetry), stabilized lattice oxygen *via* a phase compatible interface.[36] Considering structural compatibility, spinel oxides are ideal coatings for layered oxides owing to their cubic close-packed O arrays.[37] Accordingly, intense research efforts have been made to construct layered/spinel cathode materials to take advantage of high capacity and fast kinetics from Li-rich layered oxides and spinel, respectively.[38−40] Although substantial improvements of these lattice match strategies have been achieved, direct observation of the evolution for surface oxygen and transition metal during battery cycling is still missing.

Among the various oxides, the selected inverse spinel $NiFe_2O_4$ stands out for its low cost (Figure S1). For instance, moving from a $LaSrMnO_3$ coating to a $NiFe_2O_4$ coating can bring a cost decrease of 36.9%. In addition, $NiFe_2O_4$ with good Li^+-ionic conductivity has been developed as a promising anode material for lithium-ion batteries.[41−43] To date, there are no reports of $NiFe_2O_4$ coating on lithium-rich layered cathode materials. Here, we demonstrate a simple and low-cost surface treatment to form a phase compatible $NiFe_2O_4$ layer on

https://doi.org/10.1021/acsnano.1c02023
ACS Nano 2021, 15, 11607−11618

Li-rich $Li_{1.2}Ni_{0.13}Co_{0.13}Mn_{0.54}O_2$ (LNCM) cathode material *via* the coprecipitation method. The effect of a $NiFe_2O_4$-coating layer on the structure and electrochemical performance of LNCM was investigated. By combining several *in operando* and *ex situ* techniques, we direct capture surface oxygen redox decouple with cation migration. We show that this M−O−N bonding network not only suppresses O_2 release but also prevents structural degradation and Mn dissolution during electrochemical processes.

RESULTS AND DISCUSSION

The pristine LNCM and NFO-coated LNCM with coatings of 1.0, 2.0, 3.0, and 4.0 wt % NFO (denoted as NFO1, NFO2, NFO3, and NFO4, respectively) were synthesized as mentioned in the Experimental Section. Figure S2 shows the X-ray powder diffraction (XRD) patterns of LNCM before and after NFO surface treatment. All samples show diffraction peaks that can be indexed to a two-phase composite with layered structures: a hexagonal unit cell ($R\bar{3}m$, $LiMO_2$) and a monoclinic unit cell ($C/2m$, Li_2MnO_3).[6,44,45] The evident splitting of (006)/(102) and (018)/(110) is observed, suggesting the characteristic $R\bar{3}m$ layered structure.[46] It was reported that the intensity ratio of $I(003)/I(104)$ usually represents the level of Li/Ni cation mixing.[6,47] The values of $I(003)/I(104)$ for LNCM, NFO1, NFO2, NFO3, and NFO4 are 1.61, 1.68, 1.74, 1.88, and 1.82, respectively. These values are much larger than 1.2, which implies low level cation mixing.[15] The NFO3 shows the lowest Li/Ni mixing level among them. The weak peaks in the 2θ region of 20 to 25° are normally assigned to characteristic superlattice peaks owing to Li and Mn cation short-range ordering in the transition metal (TM) layer.[48] In particular, the weak diffraction peak located at 20.8° is assigned to the (020) plane of monoclinic Li_2MnO_3. After NFO surface coating, there were no obvious peak shifts in any of the samples, indicating this modification does not change the bulk crystal structure. To confirm the NFO was successfully introduced on the surface of LNCM material, we further applied the Rietveld refinement. The XRD Rietveld refinement patterns of pristine LNCM, LNCM calcined at 500 °C (LNCM-500), and NFO3 powders are shown in Figure S3. All refinements fit well with the experimental data points (R_{wp} = 6.67%, 8.08%, 6.67%, respectively). The crystallographic details deduced from the refinement are given in Table S1. The results suggest that the bulk structure of LNCM is not affected by heat treatment or the NFO-coating process. Note that the reflections result from $NiFe_2O_4$ (space group $Fd\bar{3}$ m, JCPDS entry 10-0325) can be observed, confirming the NFO coating on LNCM (inset in Figure S3c). To further investigate the surface structure, the Raman spectra of pristine LNCM and NFO3 powder are shown in Figure S4. For pristine LNCM, the Raman spectrum contains two strong peaks at around 485 and 600 cm^{-1}, which can be assigned to E_g and A_{1g} of the $R\bar{3}m$ lattice,[49] while the weak peak at ∼415 cm^{-1} represents Ag mode of Li_2MnO_3 phase.[38] After the NFO coating, the Raman spectrum shows a slight red shift, indicating probably bonding between pristine LNCM and NFO coating. The two strong peaks at 630 and 670 cm^{-1} are attributed to the characteristic of cubic spinel, suggesting the presence of NFO coating.[38,50]

The particle morphologies of pristine LNCM and NFO-coated samples are shown in Figure 1a,d and Figure S5,6. Overall, the samples display similar morphology of agglomerated primary particles with spherical secondary particles. After NFO coating, the spherical features are nearly unchanged. The surface of the particles becomes rougher with the increasing NFO amount, as observed in Figure 1d and Figure S5. Subsequently, a transmission electron microscopy (TEM) technique was used to further verify the presence of NFO coating. Figure 1b shows a typical TEM micrograph of pristine LNCM. The particle size is about 150 nm with a smooth surface. In comparison, a uniform layer is evident in NFO3 as observed in Figure 1e. The thickness of the layer is calculated to be about 15 nm. The TEM images of NFO1, NFO2, and NFO4 are shown in Figure S6. When the NFO-coating amount applied is 1 wt %, the surface remains smooth with nanoparticles anchored randomly (Figure S6a,d). As the coating amount is increased, the coating layer becomes rougher and thicker (Figure S6b,e and Figure S6c,f). Figure 1c,f show the details of the layered structure along with the phase boundary between LNCM and NFO3. Figure 1c exhibits a dihedral angle of 81.09°, corresponding to (111) and (11$\bar{1}$) planes of the monoclinic Li_2MnO_3 phase. This morphological feature is in good agreement with the single-phase Li_2MnO_3 crystal structure, as illustrated in the inset of Figure 1c and Figure S7. The NFO coating on the surface of LNCM can be observed with well-defined lattice planes spaced 0.20 and 0.24 nm apart, corresponding to (104) and (006) planes for the hexagonal $LiMO_2$ phase (Figure 1f). The calculated interfacial angle between these two planes is 55.09°, in accordance with the crystal structure of $LiMO_2$ (Figure S8). On the NFO side, the lateral LNCM/NFO heterointerface appears with a lattice spacing of 0.20 nm corresponding to the (400) plane. In the external surface, the lattice spacing of 0.25 nm belongs to the (311) plane (indicated by the pink plane in Figure S9). These interface features can be observed elsewhere, as shown in Figure S10.

In the NFO structure, the tetrahedral site is filled by half of Fe^{3+} ions, while the octahedral site is filled by Ni^{2+} and the remaining Fe^{3+} ions.[51] Compared with the phase compatible coating that we reported before,[36] there is a great difference between perovskite structure and spinel structure. However, similar to MnO_6 octahedra in $La_{0.8}Sr_{0.2}MnO_{3-y}$, NFO also has NO_6 octahedra. The octahedral N−O (N = Ni, Fe) distance in NFO structure is about 2.03 Å, similar to the octahedral M−O bond length in the $LiMO_2$ phase (1.96 Å), thereby ensuring the formation of a heterostructural O-sharing bonding between the NFO and LNCM (Figure 1g). This M−O−N interface bonding plays an important role not only in stabilizing lattice oxygen not only in the $LiMO_2$ grain boundary but also in the strengthening of the coating during electrochemical cycling (Figure 1h).

X-ray photoelectron spectroscopy (XPS) is a powerful technique for investigating the oxidation states of surface compositions with high sensitivity. Figure 1i shows the O 1s spectra of the LNCM and NFO-coated samples. In brief, the O 1s spectra in all samples are mainly composed of two peaks located at ∼529.5 and 531.5 eV, corresponding to oxide ions (O^{2-}) in the lattice and weakly carbonate species (CO_3^{2-}) on the surface, respectively (Figure 1i).[52] The main peak shifting slightly to high binding energy is observed after NFO surface treatment. For example, the O 1s spectrum of NFO3 displays three main components (Figure 1j): the one at lattice oxygen 529.5 eV is assigned to the O^{2-} anions in the MO_6 octahedra, while the one at 530.1 eV is characteristic of the O^{2-} anions in the NO_6 octahedra.[53] The fitting procedure of the experimental curve implies the presence of an additional

https://doi.org/10.1021/acsnano.1c02023
ACS Nano 2021, 15, 11607−11618

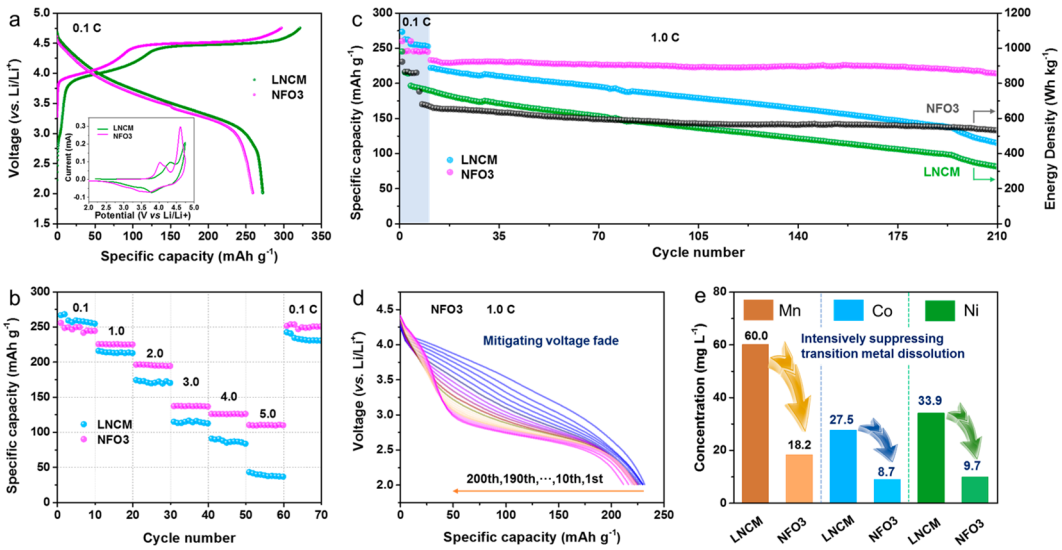

Figure 2. Electrochemical behaviors of pristine LNCM and NFO3 electrodes. (a) Galvanostatic charge−discharge profiles in the first cycle at 0.1 C (26 mAh g^{-1}) inset with CV curves. (b) Rate capability. (c) Cycle performance and energy density for 200 cycles at 1 C after ten formation activation cycles at 0.1 C. (d) Discharge profiles of NFO3. (e) Transition metal dissolution for LNCM and NFO3 electrodes after 60 cycles at 2 C.

component at ∼529.8 eV, suggesting the existence of an M−O−N bonding network. The Ni 2p, Co 2p, and Mn 2p spectra of LNCM and NFO-coated samples are shown in Figure S10. The binding energies of Ni $2p_{3/2}$ (855.2 eV) and $2p_{1/2}$ (872.8 eV), as well as two satellite peaks are observed (Figure S11a), which is the evidence of Ni^{2+}.[54] The Co $2p_{3/2}$ and $2p_{1/2}$ peaks of the samples are observed at 780.6 and 795.6 eV with a binding energy splitting of 15 eV, which confirms the oxidation state of Co^{3+} (Figure S11b).[55,56] As shown in Figure S11c, the Mn $2p_{3/2}$ and $2p_{1/2}$ XPS spectra display binding energies of 642.5 and 654.4 eV, which demonstrates the existence of Mn^{4+} in both LNCM and NFO-coated samples.[52] For Fe 2p XPS spectra, the two main peaks located at 712.2 and 724.4 eV correspond to Fe $2p_{3/2}$ and $2p_{1/2}$, which are in good agreement with the data reported on Fe^{3+}.[57] Of note, the intensity of Fe 2p XPS spectra is mildly strengthened by increasing the NFO coating (Figure S11d). The chemical composition of the pristine LNCM and NFO was analyzed by energy dispersive spectroscopy (EDS) elemental mapping. Figure S12 shows the uniform distribution of Mn, Ni, and Co elements in pristine LNCM. Similar features are also observed for Mn and Ni elements in NFO3 (Figure 1k).

The charge−discharge curves for pristine LNCM and NFO-coated samples are shown in Figure 2a and Figure S13a. In general, all cathodes display similar typical electrochemical behaviors as reported in the literature.[22,58,59] The specific charge curves of the samples exhibit a continuous slope under 4.5 V, which is related to the oxidation of Co^{3+} and Ni^{2+} to Co^{4+} and Ni^{4+}, respectively.[60] A long plateau can be observed at approximately 4.5 V, which is the characteristic O activation in Li-rich layered oxides.[59,61] Cyclic voltammetry (CV) of pristine LNCM and NFO3 were performed at a scan rate of 0.1 mV s^{-1} between open-circuit voltage and 4.75 V (inset in Figure 2a). Overall, the pristine LNCM and NFO3 show similar CV curves. The anodic peak at 4.31 V in pristine LNCM is ascribed to the $Co^{3+/4+}$ and $Ni^{2+/4+}$ redox couples,[62] while the NFO3 shows lower anodic peaks (∼4.03 and 4.19 V), which indicates different redox couples are participating in the charge storage in both materials.[15] The noticeable anodic peaks at 4.60 V for both samples represent lithium extraction and oxygen activation, which results from Li_2MnO_3 phase in $Li_{1.2}Ni_{0.13}Co_{0.13}Mn_{0.54}O_2$.[63]

Specifically, the pristine LNCM electrode delivers the highest first discharge capacity of 273.0 mAh g^{-1} at 0.1 C in these cathodes, while in the NFO-coated electrodes, NFO3 exhibits a higher first discharge capacity of 259.8 mAh g^{-1}. Moreover, the initial Coulombic efficiency (ICE) of the NFO3 electrode is 87.2%, higher than that of LNCM electrode (84.3%), indicating an improved reversible anion redox. Excellent rate capability is a further highlight of the good electrochemical performance of the NFO3 electrode (Figure 2b and Figure S13b). NFO3 shows an average discharge capacity higher than that of pristine LNCM at all rates except 0.1 C. In particular, the NFO3 electrode possesses a discharge capacity of 109.4 mA g^{-1} at 5 C, which is almost 3 times higher than that of LNCM (38.1 mAh g^{-1}). Recent important work on Li-rich layered oxides proposed that mitigating M (notably Mn) migration and tuning oxygen redox to benefit the cationic redox activity of O−Mn^{4+}/Li^+ sites will suppress phase transition as well as O_2 release.[23,64,65] In addition, the tetrahedral and octahedral positions in $NiFe_2O_4$ offer fast electronic transport, resulting in good electrical conductivity.[66] As a result, the electronic conduction at the electrode/electrolyte interface was promoted. These findings explain why NFO3 displays a better rate performance than the pristine LNCM.

Figure 2c and Figure S13c show the cycle performance of pristine LNCM and NFO-coated samples at 1 C. The NFO-coated samples exhibit higher cycling stability than the pristine LNCM. The NFO3 electrode delivers the highest discharge capacity of 232.5 mAh g^{-1} at 1 C with a capacity retention ratio of 91.8% (213.4 mAh g^{-1}). By contrast, the pristine LNCM displays only 114.5 mAh g^{-1} after 200 cycles, which is 51.5% of the initial discharge capacity at 1 C. In brief, the cycle performance of NFO3 is superior to those of inorganic coatings on Li-rich layered oxides (Tables S2). The energy density degeneration, which is linked with voltage and capacity fade, is the bottleneck of Li-rich layered oxides. Regarding

https://doi.org/10.1021/acsnano.1c02023
ACS Nano 2021, 15, 11607−11618

energy density on the electrode level (only active material was taken into account),[67,68] there is an evident difference between LNCM and NFO3 electrodes. The energy density retention has been gradually improved from 42% to 80% with an optimal amount of NFO coating after 210 charge/discharge cycles.

It is well-known that Li-rich layered oxide cathodes undergo voltage fade during the electrochemical cycling process, which is a critical obstacle in a large scale battery application. Therefore, we compared the discharge voltage profiles of pristine LNCM and NFO3 at 1 C (Figure 2d and Figure S13d). Both samples have a similar voltage fade during early cycles. The pristine LNCM electrode shows a monotonically voltage fade. A similar trend has been previously observed in Li-rich layered oxides.[7] This feature of voltage fade is partly ascribed to the continuous reduction of metal cation.[22] Of note, a plateau located at about 2.7 V is pronounced with the battery cycling. This lower plateau can be attributed to the Mn^{3+}/Mn^{4+} redox couple. In contrast, the NFO3 electrode displays distinguishable mitigation of voltage fade during later cycles, especially after 150 cycles. We note that the Mn^{3+}/Mn^{4+} redox couple has been dramatically inhibited after NFO coating, which was accompanied by reduced capacity loss. After 150 cycles (Figure S14), the NFO3 electrode shows a lower average charge voltage and higher discharge voltage, suggesting that a lower internal resistance and polarization compared to the pristine LNCM electrode. The dQ/dV curves are plotted in Figure S15. By comparing Figure S15c,d, it is obvious that the voltage decay has been effectively suppressed *via* NFO coating, suggesting enhanced structural stability of the NFO-coated LNCM.[69] To clarify the critical role of NFO at the surface, we measured the NFO between 2.00 and 4.75 V. As shown in Figure S16, the spinel-type NFO show almost negligible reversible capacity compare to LNCM. Therefore, the NFO coating mainly acts as a protection layer with good Li^+ transport path.

High-temperature performance is essential for the practical application of Li-rich oxide cathode materials. The decayed cycle performance of Li-rich layered oxides at high-temperature is mainly ascribed to the side reactions at the electrode/electrolyte interface and the electrolyte decomposition.[70] As shown in Figure S17, the pristine LNCM electrode shows poor cycle performance and severe voltage fade. In contrast, the NFO3 exhibits improved cycle performance in comparison to the pristine LNCM at elevated temperature. Notably, the voltage fade was also greatly mitigated after NFO coating. These results suggest that the M−O−N bonding network greatly suppresses TM reduction (especially disproportionation of manganese) coupled with O_2 release during cycling. To further clarify these findings, we examined the resulting electrolytes from cycled batteries with pristine LNCM and NFO3 electrodes (Figure 2e). It is clearly shown that a battery with pristine LNCM electrode displays a higher TM content, having a total amount of 60.0, 27.5, and 33.9 mg L^{-1} for Mn, Co, and Ni elements, respectively. In contrast, the amount of TM dissolution for the NFO3 sample decreased to about one-third of that for the LNCM sample, in line with the above electrochemical behaviors. The result directly shows that TM dissolution, especially Mn dissolution, has been inhibited by the NFO coating.

Since the gas O_2 mainly release during the first cycle,[71] quantifying the amount of gas O_2 after the first cycle could be direct evidence to reveal the level of O_2 release in both LNCM and NFO3 electrodes. As a mature technique, gas chromatography (GC) has been applied to quantify the gas species in lithium-ion batteries.[72,73] As shown in Figure S18, the bubble in the LNCM electrode is more pronounced than that in the NFO-coated electrode. In particular, the cumulative gas O_2 detected from the LNCM electrode was 1.22 μmol. In comparison, the gas O_2 evolved in the NFO-coated electrode was 0.56 μmol. Such an obvious difference indicates that oxygen release from the lattice was suppressed after NFO surface coating, and LNCM and NFO3 might display different oxygen activities during battery cycling as well.

Therefore, we investigated the electronic structure of manganese and oxygen using the *ex situ* XPS technique to clarify the electrochemical redox change during the first cycle. Figure 3 shows the XPS O 1s and Mn 2p spectra collected from LNCM and NFO3 electrodes throughout charge/discharge processes in the range 2.00−4.75 V. The selected points for spectra collection are plotted in Figure 3a. On

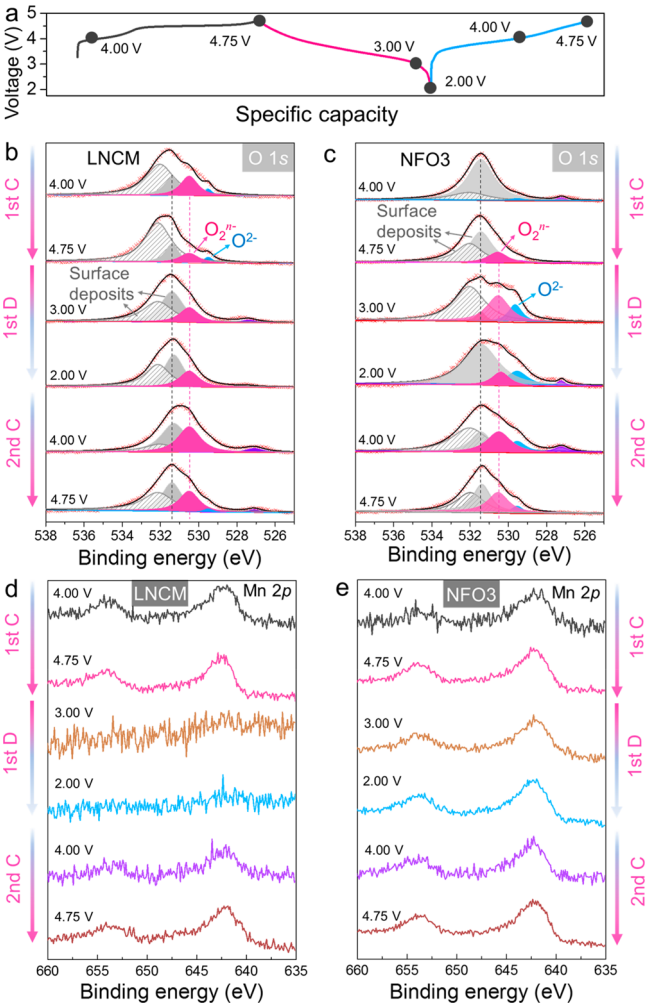

Figure 3. XPS results of pristine LNCM and NFO3 electrodes. (a) The measurements were applied to the first charge−discharge process. (b, c) Evolution of O 1s XPS spectra of LNCM and NFO3 electrodes, respectively. Red crosses are experimental data, and black curves are fits. The binding energy ∼529.5 eV corresponds to the lattice O^{2-} peak. The binding energy ∼530.5 eV represents the oxidized lattice oxygen and the O_2^{n-} component, while the binding energy ∼531.7 eV is assigned to surface deposits. An extra peak at ∼527.3 eV is assigned to lithium oxide.[77] (d, e) Evolution of Mn 2p XPS spectra of LNCM and NFO3 electrodes, respectively.

https://doi.org/10.1021/acsnano.1c02023
ACS Nano 2021, 15, 11607−11618

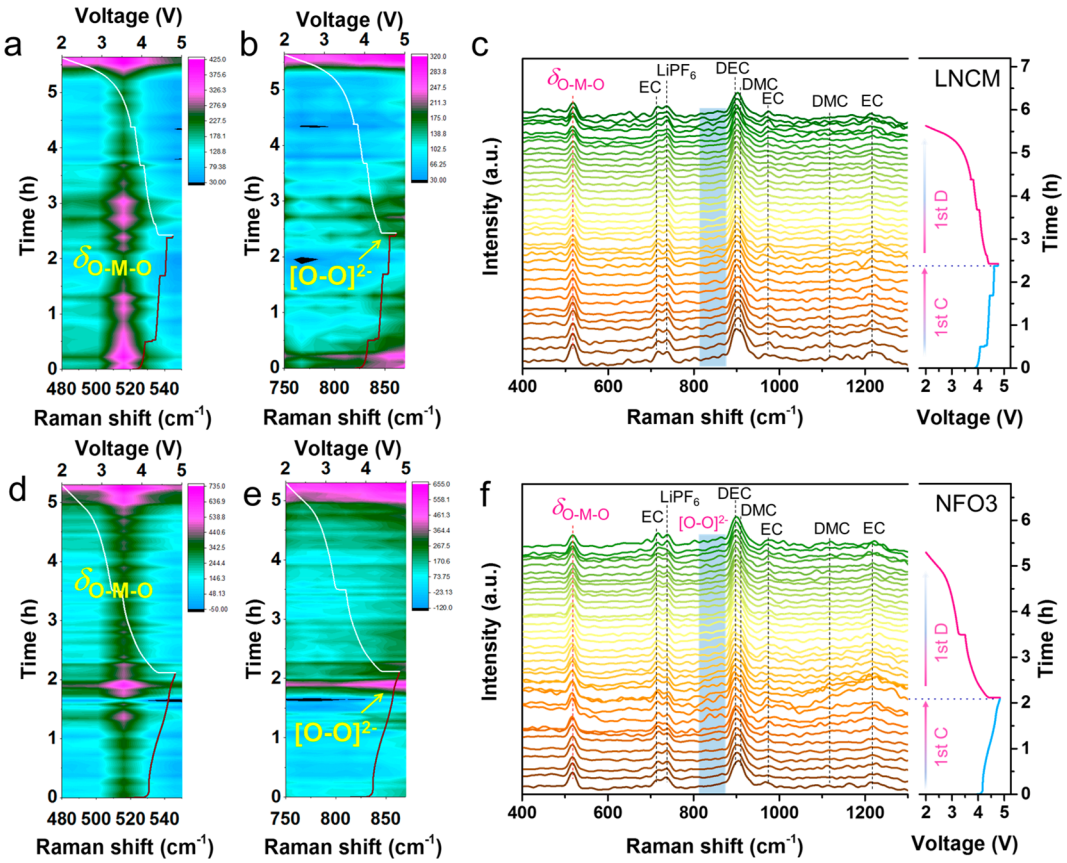

Figure 4. ***In operando*** **Raman spectral evolution for pristine LNCM and NFO3 electrodes. Evolution of the bending modes δ (O−M−O) with an A_{1g} symmetry, peroxo O−O (O_2^{2-}) bond stretching, and excerpts from the waterfall diagram of the Raman spectra for (a−c) LNCM and (d−f) NFO3 electrodes, respectively.**

charging to 4.00 V, the LNCM electrode is characterized by a weak peak at 529.5 eV owing to lattice O^{2-} (Figure 3b). A strong peak that appears on the higher binding energy side of lattice O^{2-} at 530.5 eV can be assigned to oxidized lattice O^{2-} and O_2^{n-} ($n < 2$), which is consistent with a previous report.[74] The component at ∼531.7 eV is due to the oxygenated deposited species on the surface. In particular, the degradation of organic carbonate electrolyte may generate organic oxygenated species, and their binding energies are observed in the range 531.5−534.0 eV.[75] Likewise, the inorganic species (such as phosphates, fluorophosphates, lithium salt) originating from the degradation of the $LiPF_6$ in the electrolyte are also located at higher binding energy.[76] When charging to 4.75 V, the intensity of the O_2^{n-} peak decreased in comparison to the intensities of deposited species peaks. When the electrode is operated in a discharging process, the O_2^{n-} grows slightly at the expense of lattice O^{2-}. The absence of lattice O^{2-} suggests that the lattice oxygen was in the oxidized stage during discharge processes. Besides these aspects, an interesting peak at ∼527.3 eV binding energy is observed, which is in agreement with the spectra of lithium oxide.[77] Although this peak seemed to appear rather randomly, its intensity variation during charge−discharge implies its link with anionic redox.

Turning to NFO3, the most obvious difference is the absence of the O_2^{n-} component when the first charge proceeds to 4.00 V (Figure 3c). We note that more O_2^{n-} has generated in the absence of a lattice oxygen signal (O^{2-}) when NFO3 was charged to 4.75 V. Although there is no unified understanding of oxygen redox in Li-rich layered oxides, researchers agree with the viewpoint that lattice oxygen undergoes a $O^{2-} \Leftrightarrow O_2^{n-} \Leftrightarrow O_2$redox.[5,78,79] Therefore, tuning oxygen redox means to maximize the stage $O^{2-} \Leftrightarrow O_2^{n-}$

. As shown in Figure S19, the LNCM displays a capacity contribution of 41.5% (TM oxidation) and 58.5% (O oxidation). Interestingly, the NFO3 exhibits a long plateau at high voltage with a capacity contribution of 64.3% (O oxidation). The longer O-redox plateau on charge and lower irreversible capacity loss in NFO3 compared to those of pristine LNCM suggest a higher level of $O^{2-} \Leftrightarrow O_2^{n-}$ redox after O-sharing bonding coating, consistent with the *ex situ* GC and XPS results. The peak at 530.5 eV grows on charging to 4.75 V and gradually increases when discharging to 3.00 V. Of note, the lattice O^{2-} shows a rapid growth during the discharge process and can be still observed in the second charge process. These results suggest that the phase compatible NFO coating tunes oxygen redox, especially in the first charge process. The Mn 2p XPS spectra further support this contention, as shown in Figure 3d,e. We note that two peaks at ∼642.0 and ∼654.0 eV are observed, which can be assigned to Mn $2p_{3/2}$ and $2p_{3/2}$. The LNCM shows a rougher experimental curve than that of the NFO3 electrode, indicating a thicker surface deposit layer. In particular, the intensity of Mn 2p spectra in LNCM decreased significantly with discharged to 3.00 and 2.00 V, which is in accord with a previous report.[52] In contrast, the NFO3 electrode also shows distinct Mn 2p intensity below 4.00 V. The loss of signals at 3.00 and 2.00 V is attributed to thick surface deposits. These deposited species are electro-

https://doi.org/10.1021/acsnano.1c02023
ACS Nano 2021, 15, 11607−11618

chemically stable at low potential. Upon charging, the intensity of Mn 2p recovers at 4.00 and 4.75 V, indicating that the majority of surface deposits disappear, maybe due to electrochemical decomposition at high potential. In brief, the findings from XPS spectra can be summarized *via* two aspects: (1) O-sharing bonding LNCM/NFO heterostructure trapped the oxidized lattice oxygen, tuning oxygen redox and ultimately delivering a higher specific capacity and a lower amount of O_2 release; (2) the reduced decomposition of carbonate solvent mitigated HF formation, thereby inhibiting Mn dissolution from LNCM.

Although *ex situ* XPS data provides details of chemical evolution on the surface, they do not reveal the local structural evolution. *In operando* Raman spectroscopy was carried out to further understand the correlation between electrochemical response and structural evolution of LNCM and NFO3 during cycling. Previous studies proposed that the layered $LiMO_2$ oxides with the *Rm* space group can be characterized by two Raman active modes.[80,81] One is the E_g vibration mode (O−M−O shear-like form) where oxygens in adjacent parallel layers move in opposite directions. The other is the A_{1g} vibration mode where oxygens in M−O stretch symmetrically along the *c* axis. Figure 4 shows the *in operando* Raman spectra of the LNCM and NFO3 electrodes during their first charge−discharge cycle. The peak positions and intensity trends upon cycling evidence the details of oxygen local environment tuned by M^{4+}−O.[82] The spectral features are dominated by the strong A_{1g} band at ∼517 cm^{-1} in the low-wavenumber region (400−680 cm^{-1}), as shown in Figure 4a,d. The bands centered around 517 cm^{-1} show different behaviors. Specifically, in pristine LNCM, the band is the weakest in the lithiated state (around 4.0 to 3.0 V), while in NFO3, the intensity of the band reaches maximum close to the end of delithiation. Therefore, we conclude that the oxygen local environment is different in the two oxides, which further supports the O-sharing bonding. We note that a group of weak Raman bands are located within the low-wavenumber region upon battery cycling (Figure S20). Compared with results for pristine LNCM and NFO3, the appearance of bands at 443, 570, and 632 cm^{-1} represent the most difference in Raman spectral evolution. The bands at 570 and 443 cm^{-1} are assigned to the A_{1g} and B_g modes of Li_2MnO_3 derived from the *C*2/*m* space group symmetry (Mn^{4+}−O).[83] In previous reports,[22,59] voltage fade in Li-rich layered oxides were attributed to oxygen surrounded by Mn^{4+} and Li^+ ions (O−Mn^{4+}/Li^+) electron hole localization and activating lower-voltage Mn^{3+}/Mn^{4+} redox couples. The (570, 443) cm^{-1} pair is the strongest at the end of lithiation, indicating a high level of Mn^{3+}/Mn^{4+} redox couples in pristine LNCM. On the contrary, this pair of bands were not pronounced in NFO3. Therefore, this finding explains the NFO-coating-suppressed voltage fade during the lower voltage stage. In addition, the new band at 632 cm^{-1} in NFO3 is characteristic of Li-vacancy formation.[82]

Oxygen redox couples with TM cationic redox are used to explain electrochemistry in Li-rich layered oxides. Accordingly, peroxo-like species are likely to be formed in Li-rich layered oxides during charging.[84] Interestingly, a couple of new bands at ∼850 cm^{-1} appear once the voltage reaches 4.5 V and gradually become weaker during the subsequent discharging in NFO3, which is not notable in pristine LNCM (Figure 4b,e). These bands can be ascribed to peroxo O−O (O_2^{2-}) bond stretching, resulting from reversible oxygen redox in Li-rich layered oxides.[85] A similar trend is not observed in pristine LNCM. This indicates that peroxo-like species are probably oxidized to oxygen gas, consistent with the GC and *ex situ* XPS results. Taking the δ(O−M−O) and peroxo O−O bond stretching into account, we found they have almost the same Raman spectral evolution (Figure 4d,e). In this case, links between TM/Li arrangement in the TM layer and the formation/dissociation of peroxo O−O bond can be reasonably unified together. Coupling between oxygen redox and cation migration has been proposed to explain cation/anion redox chemistry in Li-rich layered oxides in which overoxidation of the TM ions triggers O oxidation and formation of peroxo-like O−O dimers.[86−88] This structure-redox coupled process [$(O^{2-} + TM) \rightarrow (O^- + TM_{migration})$] is attributed to a striking change in the local O coordination environment. When applied NFO coating, the M−O−N bonding greatly suppressed transition metal reduction (especially disproportionation of Mn) coupled with oxygen release during cycling, resulting from higher cationic redox activity of O−Mn^{4+}/Li^+ sites. This direct visualization of surface oxygen redox decouple with cation migration explains why reversible oxygen redox can be achieved after phase compatible NFO coating. In particular, nonbonding coordination of surface oxygen has been avoided by M−O−N bonding network. Thus, surface oxygen-cationic vacancy undercoordination can be inhibited, in line with previously reported data.[89] In the midwavenumber region (680−1300 cm^{-1}), the Raman bands undergo similar evolution in both pristine LNCM and NFO3 (Figure 4c,f). Our results are consistent with Raman spectra of the $LiPF_6$-salt electrolyte.[90,91]

Previous studies on Li-rich layered oxide cathodes proposed that battery degradation upon long-term electrochemical cycling is a result of structural changes, including layered to spinel transitions,[92] generation of defects, and nanovoids.[23,93] Therefore, *ex situ* TEM analysis was performed to visualize the localized structural rearrangements on surfaces. Figure 5a shows a typical layered atomic column with simultaneous amorphous (white dash lines) and nanovoid domains (yellow dotted circles). A surface spinel-like layer is observed, where the white dashed line and yellow dashed line indicate the boundary of the spinel phase and layered phases, respectively (Figure 5b). These findings suggest that the LNCM electrode undergoes critical TM cation migration and O_2 release during extended cycling. The structure degradation is suppressed in bulk LNCM after NFO-coating, indicating higher structural stability of NFO3 electrodes than of LNCM electrodes. The LNCM/NFO lateral heterostructure is still observed in the form of parallel planes between (104) and (400) planes (Figure 5c). A similar heterostructure is also observed between the (006) plane in LNCM and the (311) plane in NFO (Figure 5d). The superior structural stability of NFO-coated LNCM was further confirmed by *ex situ* XRD analysis (Figure S21). Considering that the $R\bar{3}$ *m* phase accounts for the majority of the active material (Table S3), we accordingly investigated the Li/Ni mixing in the $R\bar{3}$ *m* phase of LNCM. It is found that 9.2(2)% of Li sites in Li slabs were occupied by Ni in LNCM after prolonged cycling, whereas the value decreased to 3.2(3)% in the NFO3 counterpart, confirming that the Li/Ni mixing was significantly mitigated by NFO coating. On the basis of the comparisons above, we can conclude that the heterostructural O-sharing bonding between LNCM and NFO plays a critical role in enhancing structural

https://doi.org/10.1021/acsnano.1c02023
ACS Nano 2021, 15, 11607−11618

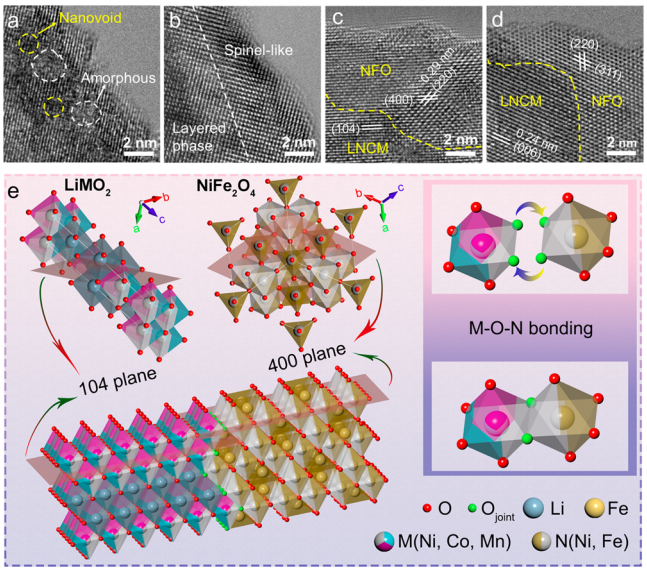

Figure 5. HRTEM images of local structure for LNCM and NFO3 electrodes. All electrodes were operated in a acharge/discharge process after 200 cycles at 1 C rate. (a, b) LNCM electrode and (c, d) NFO3 electrodes, respectively. (e) Schematic of the heterostructural O-sharing bonding of LNCM (104 plane) and NFO (400 plane).

stability as well as electrochemical performance. A full understanding of the O-sharing bonding mechanism is illustrated in Figure 5e and Figure S22. According to a previous report, all the layered, rock-salt, and spinel phases possess a cubic close-packed oxygen lattice.[65] Bond-length contraction can lead to charge transfer from dangling oxygens to the metal bonding partners.[79] The surface M−O in MO_6 and N−O bonds in NO_6 octahedra are expected fractures during synthesis. As a consequence, vacant O sites are generated. The vacant O sites are supposed to subsequently bond and hence form the M−O−N bonding between the (104) and (400) planes.

Such a heterostructural O-sharing coating presents three positive features: (1) The O-sharing bonds stabilize the surface lattice oxygens. Thus, irreversible oxygen redox in the form of O_2^{n-}/O_2 can be suppressed, resulting in decreased voltage fade and enhanced first-cycle reversible. (2) Simultaneously, cation migration into Li sites, which is coupled with oxygen redox,[87] is therefore mitigated. Consequently, they inhibit the layered-spinel transition and formation of M_{Li}−V_M defects during cycling. (3) Lastly, side reactions such as Mn dissolution can be inhibited through this phase compatible surface coating.

CONCLUSIONS

We developed a facile strategy to form a heterostructural surface coating through M−O−N bonding. Instead of surface M−O and N−O bonds, the surface regions of LNCM and NFO share a fully bonded oxygen framework. The M−O−N axes configurations are suggested to (1) impede adjacent surface lattice oxygen from participating in anion redox, which is expected to initiate at the surface, and (2) impede structural collapse during the process of Li deinsertion. More importantly, we direct capture the evolution of surface oxygen decouple with cation migration through *in operando* Raman spectroscopy. By optimizing the NFO-coating amount, high cycle stability (91.8% at 1 C after 200 cycles) and rate capability (109.4 mA g^{-1} at 1 C) were obtained for NFO3. Our results suggest a feasible strategy to design an effective surface coating for tuning oxygen redox in Li-rich layered oxides.

EXPERIMENTAL SECTION

Synthesis of LNCM Materials. LNCM was synthesized by coprecipitation as we reported previously.[36] Typically, stoichiometric $MnSO_4{\cdot}H_2O$, $CoSO_4{\cdot}H_2O$, and $NiSO_4{\cdot}6H_2O$ with Mn/Co/Ni molar ratio 5.4:1.3:1.3 were dissolved in distilled water with continuous stirring to produce a 1.0 M solution. The above solution was then added to a 2.0 M NaOH aqueous solution with vigorous stirring under a N_2 atmosphere. The pH value was kept to 11 with NH_4OH. Subsequently, the precipitate was filtered, washed, and dried in a vacuum oven at 80 °C for 24 h. After that, this hydroxide precursor was mixed and ball-milled with stoichiometric Li_2CO_3 and then calcined at 900 °C for 12 h in air.

Synthesis of NFO-Coated LNCM Materials. NFO material for surface coating was synthesized *via* a coprecipitation method with details as follows: The Li-rich powder was dispersed in a 100 mL NH_4OH solution by turbulent stirring at 80 °C for 3 h. Then, stoichiometric $Fe(NO_3)_3{\cdot}9H_2O$ and $Ni(NO_3)_2{\cdot}6H_2O$ aqueous solutions were added dropwise with strong stirring for 1 h. The pH value was adjusted to 9 to obtain homogeneous hydroxides. After being washed with distilled water several times, the mixture was calcined at 500 °C for 4 h under N_2 gas to obtain the $NiFe_2O_4$ coated Li-rich $Li_{1.2}Ni_{0.13}Co_{0.13}Mn_{0.54}O_2$ powders. The weight ratios of NFO on the coated samples were 1.0, 2.0, 3.0, and 4.0 wt %, respectively. For comparison, LNCM without coating was also calcined at 500 °C, termed LNCM-500.

Materials Characterization. The elemental composition of the pristine LNCM and NFO3 powder were analyzed by inductively coupled plasma-atomic emission spectrometry (ICP-AES, iCAP PRO, Thermo Scientific; Table S4). XRD data were collected on a Rigaku D/Max 2500 V/PC X-ray diffractometer with Cu Kα radiation (λ = 1.5406 Å, 40 kV, 50 mA) at scan rates of 2° min^{-1} and 0.5° min^{-1} (for Rietveld refinement). Morphological studies were observed by using field emission SEM (FEI Quanta 200) and transmission electron microscopy (JEOL-2010F). High-resolution morphological features and elemental analyses were conducted by high-angle annular dark-field and annular bright-field scanning transmission electron microscopy (HAADF-STEM, ABF-STEM, JEM-ARM200F) at a beam voltage of 200 kV with attached EDS (NORAN System7, Thermo Scientific). The oxidation states of transition metals (TM) were measured using XPS (ESCALAB 250Xi, Thermo Scientific). *In operando* Raman measurement was performed on a Raman spectrometer (inVia, Renishaw) with a 514 nm wavelength laser, a laser beam of ∼1 μm beam diameter, and 1 mW power. The cycled batteries were opened, and surplus electrolytes were analyzed by ICP-AES.

Electrochemical Test. To fabricate the electrode, the pristine LNCM and NFO-coated LNCM powders as active materials (80 wt %), super P (10 wt %) as a conductive agent, and poly(vinylidene fluoride) (10 wt %) as a binder were mixed with *N*-methyl-2-pyrrolidone (NMP) to form a slurry. The homogeneous slurry was then cast onto aluminum foil, followed by drying at 80 °C for 12 h in a vacuum oven. The mass loading of active material was ∼10 mg cm^{-2} with a compacted density of ∼3.7 g cm^{-3}. Next, the material loaded foil was cut into round cathodes with a diameter of 1.0 cm. Finally, CR2032 coin cells were assembled in an argon-filled glovebox by using Li foil as an anode, 1 M lithium hexafluorophosphate ($LiPF_6$) in ethylene carbonate (EC), diethyl carbonate (DEC), and dimethyl carbonate (DMC) solution (volumetric 1:1:1) as the electrolyte, and polypropylene membranes (Celgard 2400) as a separator. Before electrochemical processes, each cell was aged for 12 h to ensure ample soaking of the electrolyte into the electrode and separator. Electrochemical measurement was performed on a LAND CT-2001A cycler between 2.00 and 4.75 V at 25 °C temperature. The C-rate is defined on the basis of 1 C = 260 mA g^{-1}. For the postcycled

https://doi.org/10.1021/acsnano.1c02023
ACS Nano 2021, 15, 11607−11618

morphology characterization, active materials were scraped from the electrodes and then washed in DMC before being loaded onto holey carbon grids. The *ex situ* XRD measurement was collected from cycled electrodes with Al foil. Cyclic voltammetry (CV) curves were collected on an electrochemical workstation (Zahner IM6) at 0.1 mV s^{-1} in the range 2.00−4.75 V.

Gas O_2 Amount Test. The released gas O_2 was detected *ex situ* by GC (Agilent 7890B) using an internal standard method. Argon was selected as a carrier gas at a flow rate of 25 mL min^{-1}. To realize the GC measurement, each cathode cell was punched a hole. These CR2032 coin cells were assembled and tested for one cycle at 0.1 C between 2.00 and 4.75 V. The discharged cells were transferred to a nitrogen-filled glovebox for gas collection. Finally, the gas species in the cycled cell were collected by a syringe sampler.

ASSOCIATED CONTENT

Supporting Information

The Supporting Information is available free of charge at https://pubs.acs.org/doi/10.1021/acsnano.1c02023.

Estimated costs of several coating materials; chemical compositions; ICP-AES results; XRD patterns; crystallographic data and structures; Raman spectra; SEM and TEM images; XPS spectra; STEM-EDS elemental mapping; electrochemical performance of NFO-coated LNCM; electrochemical performance comparison; average charge and discharge voltage, voltage vs specific capacity profiles, and Q/dV curves of LNCM and NFO3; XRD pattern and voltage profile of pure NFO; electrochemical performance of LNCM and NFO3 electrode at 55 °C; GC profiles of gas components collected from LNCM and NFO3 electrodes; excerpts from Raman spectra of LNCM and NFO3; *ex situ* XRD patterns (PDF)

AUTHOR INFORMATION

Corresponding Authors

Sijiang Hu − *Guangxi Key Laboratory of Low Carbon Energy Materials, School of Chemical and Pharmaceutical Sciences, Guangxi Normal University, Guilin 541004, P. R. China; Hubei Key Laboratory for Processing and Application of Catalytic Materials, College of Chemical Engineering, Huanggang Normal University, Huanggang 438000, P. R. China;* orcid.org/0000-0002-1254-9514; Email: sjhu@gxnu.edu.cn

Hongqiang Wang − *Guangxi Key Laboratory of Low Carbon Energy Materials, School of Chemical and Pharmaceutical Sciences, Guangxi Normal University, Guilin 541004, P. R. China;* orcid.org/0000-0002-9684-8609; Email: whq74@gxnu.edu.cn

Zaiping Guo − *School of Chemical Engineering & Advanced Materials, The Unveristy of Adelaide, Adelaide 5005, Australia;* orcid.org/0000-0003-3464-5301; Email: zaiping.guo@adelaide.edu.au

Authors

Jiming Peng − *Guangxi Key Laboratory of Low Carbon Energy Materials, School of Chemical and Pharmaceutical Sciences, Guangxi Normal University, Guilin 541004, P. R. China; Hubei Key Laboratory for Processing and Application of Catalytic Materials, College of Chemical Engineering, Huanggang Normal University, Huanggang 438000, P. R. China*

Yu Li − *Guangxi Key Laboratory of Low Carbon Energy Materials, School of Chemical and Pharmaceutical Sciences, Guangxi Normal University, Guilin 541004, P. R. China;* orcid.org/0000-0002-3431-8266

Zhiqiang Chen − *Guangxi Key Laboratory of Low Carbon Energy Materials, School of Chemical and Pharmaceutical Sciences, Guangxi Normal University, Guilin 541004, P. R. China*

Gemeng Liang − *Institute for Superconducting and Electronic Materials, School of Mechanical, Materials, Mechatronic and Bio-medical Engineering, University of Wollongong, Wollongong 2500, Australia*

Tengfei Zhou − *Institutes of Physical Science and Information Technology, Key Laboratory of Structure and Functional Regulation of Hybrid Material (Ministry of Education), Anhui Graphene Engineering Laboratory, Anhui University, Hefei 230601, China;* orcid.org/0000-0002-7364-0434

Fenghua Zheng − *Guangxi Key Laboratory of Low Carbon Energy Materials, School of Chemical and Pharmaceutical Sciences, Guangxi Normal University, Guilin 541004, P. R. China;* orcid.org/0000-0001-7522-4728

Qichang Pan − *Guangxi Key Laboratory of Low Carbon Energy Materials, School of Chemical and Pharmaceutical Sciences, Guangxi Normal University, Guilin 541004, P. R. China;* orcid.org/0000-0003-0418-0240

Qingyu Li − *Guangxi Key Laboratory of Low Carbon Energy Materials, School of Chemical and Pharmaceutical Sciences, Guangxi Normal University, Guilin 541004, P. R. China;* orcid.org/0000-0003-4638-4401

Jianwen Liu − *College of Chemistry and Chemical Engineering, Hubei University, Wuhan 430062, P. R. China; China Jiangsu Pylon Battery Co. Ltd., Yangzhou 211400, P. R. China;* orcid.org/0000-0003-4929-1075

Complete contact information is available at: https://pubs.acs.org/10.1021/acsnano.1c02023

Author Contributions

○J.P. and Y.L. contributed equally to this work.

Notes

The authors declare no competing financial interest.

ACKNOWLEDGMENTS

We acknowledge the support from the National Natural Science Foundation of China (Grant Nos. 51902108, 51762006, 51802357, and 51774100), Guangxi Technology Base and Talent Subject (Grant No. GUIKE AD20297086), Guangxi Innovation Driven Development Subject (Grant No. GUIKE AA19182020), Guangxi Natural Science Foundation (Grant No. 2018GXNSFBA138002), Guangxi Technology Base and Talent Subject (Grant No. GUIKE AD18126001), and Special Fund for Guangxi Distinguished Expert. G.M.L. acknowledges the Australian Institute of Nuclear Science and Engineering (AINSE) Limited for financial assistance in the form of a Post Graduate Research Award (PGRA).

REFERENCES

(1) Liang, G.; Wu, Z.; Didier, C.; Zhang, W.; Cuan, J.; Li, B.; Ko, K.-Y.; Hung, P.-Y.; Lu, C.-Z.; Chen, Y.; Leniec, G.; Kaczmarek, S. M.; Johannessen, B.; Thomsen, L.; Peterson, V. K.; Pang, W. K.; Guo, Z. A Long Cycle-Life High-Voltage Spinel Lithium-Ion Battery Electrode Achieved by Site-Selective Doping. *Angew. Chem., Int. Ed.* **2020**, *59*, 10594−10602.

(2) Liu, Y.; Tai, Z.; Zhou, T.; Sencadas, V.; Zhang, J.; Zhang, L.; Konstantinov, K.; Guo, Z.; Liu, H. K. An All-Integrated Anode *via* Interlinked Chemical Bonding between Double-Shelled-Yolk-Struc-

tured Silicon and Binder for Lithium-Ion Batteries. *Adv. Mater.* **2017**, *29*, 1703028.
(3) Lou, S.; Zhao, Y.; Wang, J.; Yin, G.; Du, C.; Sun, X. Ti-Based Oxide Anode Materials for Advanced Electrochemical Energy Storage: Lithium/Sodium Ion Batteries and Hybrid Pseudocapacitors. *Small* **2019**, *15*, 1904740.
(4) Schmuch, R.; Wagner, R.; Hörpel, G.; Placke, T.; Winter, M. Performance and Cost of Materials for Lithium-Based Rechargeable Automotive Batteries. *Nat. Energy* **2018**, *3*, 267−278.
(5) Assat, G.; Tarascon, J.-M. Fundamental Understanding and Practical Challenges of Anionic Redox Activity in Li-Ion Batteries. *Nat. Energy* **2018**, *3*, 373−386.
(6) Thackeray, M. M.; Kang, S.-H.; Johnson, C. S.; Vaughey, J. T.; Benedek, R.; Hackney, S. A. Li_2MnO_3-Stabilized $LiMO_2$ (M = Mn, Ni, Co) Electrodes for Lithium-Ion Batteries. *J. Mater. Chem.* **2007**, *17*, 3112−3125.
(7) Hu, S.; Pillai, A. S.; Liang, G.; Pang, W. K.; Wang, H.; Li, Q.; Guo, Z. Li-Rich Layered Oxides and Their Practical Challenges: Recent Progress and Perspectives. *Electrochem. Energy Rev.* **2019**, *2*, 277−311.
(8) Yin, W.; Grimaud, A.; Rousse, G.; Abakumov, A. M.; Senyshyn, A.; Zhang, L.; Trabesinger, S.; Iadecola, A.; Foix, D.; Giaume, D.; Tarascon, J.-M. Structural Evolution at the Oxidative and Reductive Limits in the First Electrochemical Cycle of $Li_{1.2}Ni_{0.13}Mn_{0.54}Co_{0.13}O_2$. *Nat. Commun.* **2020**, *11*, 1252.
(9) Zhu, Z.; Yu, D.; Yang, Y.; Su, C.; Huang, Y.; Dong, Y.; Waluyo, I.; Wang, B.; Hunt, A.; Yao, X.; Lee, J.; Xue, W.; Li, J. Gradient Li-Rich Oxide Cathode Particles Immunized Against Oxygen Release by a Molten Salt Treatment. *Nat. Energy* **2019**, *4*, 1049−1058.
(10) Zhao, E.; Li, Q.; Meng, F.; Liu, J.; Wang, J.; He, L.; Jiang, Z.; Zhang, Q.; Yu, X.; Gu, L.; Yang, W.; Li, H.; Wang, F.; Huang, X. Stabilizing the Oxygen Lattice and Reversible Oxygen Redox Chemistry through Structural Dimensionality in Lithium-Rich Cathode Oxides. *Angew. Chem., Int. Ed.* **2019**, *58*, 4323−4327.
(11) Shin, Y.; Kan, W. H.; Aykol, M.; Papp, J. K.; McCloskey, B. D.; Chen, G.; Persson, K. A. Alleviating Oxygen Evolution from Li-Excess Oxide Materials through Theory-Guided Surface Protection. *Nat. Commun.* **2018**, *9*, 4597.
(12) Koga, H.; Croguennec, L.; Ménétrier, M.; Mannessiez, P.; Weill, F.; Delmas, C. Different Oxygen Redox Participation for Bulk and Surface: A Possible Global Explanation for the Cycling Mechanism of $Li_{1.20}Mn_{0.54}Co_{0.13}Ni_{0.13}O_2$. *J. Power Sources* **2013**, *236*, 250−258.
(13) Li, B.; Yan, H.; Zuo, Y.; Xia, D. Tuning the Reversibility of Oxygen Redox in Lithium-Rich Layered Oxides. *Chem. Mater.* **2017**, *29*, 2811−2818.
(14) Radin, M. D.; Vinckeviciute, J.; Seshadri, R.; Van der Ven, A. Manganese Oxidation as the Origin of the Anomalous Capacity of Mn-Containing Li-Excess Cathode Materials. *Nat. Energy* **2019**, *4*, 639−646.
(15) Qing, R.-P.; Shi, J.-L.; Xiao, D.-D.; Zhang, X.-D.; Yin, Y.-X.; Zhai, Y.-B.; Gu, L.; Guo, Y.-G. Enhancing the Kinetics of Li-Rich Cathode Materials through the Pinning Effects of Gradient Surface Na^+ Doping. *Adv. Energy Mater.* **2016**, *6*, 1501914.
(16) Wang, Y.; Gu, H.-T.; Song, J.-H.; Feng, Z.-H.; Zhou, X.-B.; Zhou, Y.-N.; Wang, K.; Xie, J.-Y. Suppressing Mn Reduction of Li-Rich Mn-Based Cathodes by F-Doping for Advanced Lithium-Ion Batteries. *J. Phys. Chem. C* **2018**, *122*, 27836−27842.
(17) Yu, Y.; Yang, Z.; Zhong, J.; Liu, Y.; Li, J.; Wang, X.; Kang, F. A Simple Dual-Ion Doping Method for Stabilizing Li-Rich Materials and Suppressing Voltage Decay. *ACS Appl. Mater. Interfaces* **2020**, *12*, 13996−14004.
(18) Billaud, J.; Sheptyakov, D.; Sallard, S.; Leanza, D.; Talianker, M.; Grinblat, J.; Sclar, H.; Aurbach, D.; Novák, P.; Villevieille, C. Li/Fe Substitution in Li-rich Ni, Co, Mn Oxides for Enhanced Electrochemical Performance as Cathode Materials. *J. Mater. Chem. A* **2019**, *7*, 15215−15224.
(19) Guan, P.; Zhou, L.; Yu, Z.; Sun, Y.; Liu, Y.; Wu, F.; Jiang, Y.; Chu, D. Recent Progress of Surface Coating on Cathode Materials for High-Performance Lithium-Ion Batteries. *J. Energy Chem.* **2020**, *43*, 220−235.
(20) Qiu, B.; Yin, C.; Xia, Y.; Liu, Z. Synthesis of Three-Dimensional Nanoporous Li-Rich Layered Cathode Oxides for High Volumetric and Power Energy Density Lithium-Ion Batteries. *ACS Appl. Mater. Interfaces* **2017**, *9*, 3661−3666.
(21) Lan, X.; Li, Y.; Guo, S.; Yu, L.; Xin, Y.; Liu, Z.; Hu, X. Stabilizing Li-rich Layered Cathode Materials by Nanolayer-Confined Crystal Growth for Li-Ion Batteries. *Electrochim. Acta* **2020**, *333*, 135466.
(22) Hu, E.; Yu, X.; Lin, R.; Bi, X.; Lu, J.; Bak, S.; Nam, K.-W.; Xin, H. L.; Jaye, C.; Fischer, D. A.; Amine, K.; Yang, X.-Q. Evolution of Redox Couples in Li- and Mn-rich Cathode Materials and Mitigation of Voltage Fade by Reducing Oxygen Release. *Nat. Energy* **2018**, *3*, 690−698.
(23) Yan, P.; Zheng, J.; Tang, Z.-K.; Devaraj, A.; Chen, G.; Amine, K.; Zhang, J.-G.; Liu, L.-M.; Wang, C. Injection of Oxygen Vacancies in the Bulk Lattice of Layered Cathodes. *Nat. Nanotechnol.* **2019**, *14*, 602−608.
(24) Sharifi-Asl, S.; Yurkiv, V.; Gutierrez, A.; Cheng, M.; Balasubramanian, M.; Mashayek, F.; Croy, J.; Shahbazian-Yassar, R. Revealing Grain-Boundary-Induced Degradation Mechanisms in Li-Rich Cathode Materials. *Nano Lett.* **2020**, *20*, 1208−1217.
(25) Yu, H.; Gao, Y.; Liang, X. Slightly Fluorination of Al_2O_3 ALD Coating on $Li_{1.2}Mn_{0.54}Co_{0.13}Ni_{0.13}O_2$ Electrodes: Interface Reaction to Create Stable Solid Permeable Interphase Layer. *J. Electrochem. Soc.* **2019**, *166*, A2021−A2027.
(26) Zhang, X.; Belharouak, I.; Li, L.; Lei, Y.; Elam, J. W.; Nie, A.; Chen, X.; Yassar, R. S.; Axelbaum, R. L. Structural and Electrochemical Study of Al_2O_3 and TiO_2 Coated $Li_{1.2}Ni_{0.13}Mn_{0.54}Co_{0.13}O_2$ Cathode Material Using ALD. *Adv. Energy Mater.* **2013**, *3*, 1299−1307.
(27) Wang, Z.; Liu, E.; Guo, L.; Shi, C.; He, C.; Li, J.; Zhao, N. Cycle Performance Improvement of Li-Rich Layered Cathode Material $Li[Li_{0.2}Mn_{0.54}Ni_{0.13}Co_{0.13}]O_2$ by ZrO_2 coating. *Surf. Coat. Technol.* **2013**, *235*, 570−576.
(28) Ding, X.; Li, Y.-X.; Chen, F.; He, X.-D.; Yasmin, A.; Hu, Q.; Wen, Z.-Y.; Chen, C.-H. *in Situ* Formation of LiF Decoration on a Li-Rich Material for Long-Cycle Life and Superb Low-Temperature Performance. *J. Mater. Chem. A* **2019**, *7*, 11513−11519.
(29) Zhao, T.; Li, L.; Chen, R.; Wu, H.; Zhang, X.; Chen, S.; Xie, M.; Wu, F.; Lu, J.; Amine, K. Design of Surface Protective Layer of LiF/FeF_3 Nanoparticles in Li-rich Cathode for High-Capacity Li-Ion Batteries. *Nano Energy* **2015**, *15*, 164−176.
(30) Rosina, K. J.; Jiang, M.; Zeng, D.; Salager, E.; Best, A. S.; Grey, C. P. Structure of Aluminum Fluoride Coated $Li[Li_{1/9}Ni_{1/3}Mn_{5/9}]O_2$ Cathodes for Secondary Lithium-Ion Batteries. *J. Mater. Chem.* **2012**, *22*, 20602−20610.
(31) Zhang, X.; Yu, R.; Huang, Y.; Wang, X.; Wang, Y.; Wu, B.; Liu, Z.; Chen, J. The Influences of Surface Coating Layers on the Properties of Layered/Spinel Heterostructured Li-Rich Cathode Material. *ACS Sustainable Chem. Eng.* **2018**, *6*, 12969−12979.
(32) Xiao, B.; Wang, B.; Liu, J.; Kaliyappan, K.; Sun, Q.; Liu, Y.; Dadheech, G.; Balogh, M. P.; Yang, L.; Sham, T.-K.; Li, R.; Cai, M.; Sun, X. Highly Stable $Li_{1.2}Mn_{0.54}Co_{0.13}Ni_{0.13}O_2$ Enabled by Novel Atomic Layer Deposited $AlPO_4$ Coating. *Nano Energy* **2017**, *34*, 120−130.
(33) Si, M.; Wang, D.; Zhao, R.; Pan, D.; Zhang, C.; Yu, C.; Lu, X.; Zhao, H.; Bai, Y. Local Electric-Field-Driven Fast Li Diffusion Kinetics at the Piezoelectric $LiTaO_3$ Modified Li-Rich Cathode-Electrolyte Interphase. *Adv. Sci.* **2020**, *7*, 1902538.
(34) Zhang, H.; Yang, T.; Han, Y.; Song, D.; Shi, X.; Zhang, L.; Bie, L. Enhanced Electrochemical Performance of $Li_{1.2}Ni_{0.13}Co_{0.13}Mn_{0.54}O_2$ by Surface Modification with the Fast Lithium-Ion Conductor Li-La-Ti-O. *J. Power Sources* **2017**, *364*, 272−279.
(35) Martha, S. K.; Nanda, J.; Kim, Y.; Unocic, R. R.; Pannala, S.; Dudney, N. J. Solid Electrolyte Coated High Voltage Layered-Layered

https://doi.org/10.1021/acsnano.1c02023
ACS Nano 2021, 15, 11607−11618

Lithium-Rich Composite Cathode: $Li_{1.2}Mn_{0.525}Ni_{0.175}Co_{0.1}O_2$. *J. Mater. Chem. A* **2013**, *1*, 5587−5595.
(36) Hu, S.; Li, Y.; Chen, Y.; Peng, J.; Zhou, T.; Pang, W. K.; Didier, C.; Peterson, V. K.; Wang, H.; Li, Q.; Guo, Z. Insight of a Phase Compatible Surface Coating for Long-Durable Li-Rich Layered Oxide Cathode. *Adv. Energy Mater.* **2019**, *9*, 1901795.
(37) Luo, D.; Li, G.; Fu, C.; Zheng, J.; Fan, J.; Li, Q.; Li, L. A New Spinel-Layered Li-Rich Microsphere as a High-Rate Cathode Material for Li-Ion Batteries. *Adv. Energy Mater.* **2014**, *4*, 1400062.
(38) Zhang, X.-D.; Shi, J.-L.; Liang, J.-Y.; Yin, Y.-X.; Zhang, J.-N.; Yu, X.-Q.; Guo, Y.-G. Suppressing Surface Lattice Oxygen Release of Li-Rich Cathode Materials *via* Heterostructured Spinel $Li_4Mn_5O_{12}$ Coating. *Adv. Mater.* **2018**, *30*, 1801751.
(39) Xu, M.; Fei, L.; Lu, W.; Chen, Z.; Li, T.; Liu, Y.; Gao, G.; Lai, Y.; Zhang, Z.; Wang, P.; Huang, H. Engineering Hetero-Epitaxial Nanostructures with Aligned Li-Ion Channels in Li-Rich Layered Oxides for High-Performance Cathode Application. *Nano Energy* **2017**, *35*, 271−280.
(40) Zhang, W.; Sun, Y.; Deng, H.; Ma, J.; Zeng, Y.; Zhu, Z.; Lv, Z.; Xia, H.; Ge, X.; Cao, S.; Xiao, Y.; Xi, S.; Du, Y.; Cao, A.; Chen, X. Dielectric Polarization in Inverse Spinel-Structured Mg_2TiO_4 Coating to Suppress Oxygen Evolution of Li-Rich Cathode Materials. *Adv. Mater.* **2020**, *32*, 2000496.
(41) Xiao, Y.; Zai, J.; Tian, B.; Qian, X. Formation of $NiFe_2O_4$/Expanded Graphite Nanocomposites with Superior Lithium Storage Properties. *Nano-Micro Lett.* **2017**, *9*, 34.
(42) Jin, R.; Jiang, H.; Sun, Y.; Ma, Y.; Li, H.; Chen, G. Fabrication of $NiFe_2O_4$/C Hollow Spheres Constructed by Mesoporous Nanospheres for High-Performance Lithium-Ion Batteries. *Chem. Eng. J.* **2016**, *303*, 501−510.
(43) Zou, Y.; Li, Z.; Liu, Y.; Duan, J.; Long, B. Coaxial Structure of $NiFe_2O_4$/CNTs Composites as Anodes for Enhanced Lithium Ion Batteries. *J. Alloys Compd.* **2020**, *820*, 153085.
(44) Hong, J.; Gwon, H.; Jung, S.-K.; Ku, K.; Kang, K. Review-Lithium-Excess Layered Cathodes for Lithium Rechargeable Batteries. *J. Electrochem. Soc.* **2015**, *162*, A2447−A2467.
(45) Yu, H.; Ishikawa, R.; So, Y.-G.; Shibata, N.; Kudo, T.; Zhou, H.; Ikuhara, Y. Direct Atomic-Resolution Observation of Two Phases in the $Li_{1.2}Mn_{0.567}Ni_{0.166}Co_{0.067}O_2$ Cathode Material for Lithium-Ion Batteries. *Angew. Chem., Int. Ed.* **2013**, *52*, 5969−5973.
(46) Pang, W. K.; Lin, H.-F.; Peterson, V. K.; Lu, C.-Z.; Liu, C.-E.; Liao, S.-C.; Chen, J.-M. Effects of Fluorine and Chromium Doping on the Performance of Lithium-Rich $Li_{1+x}MO_2$ (M = Ni, Mn, Co) Positive Electrodes. *Chem. Mater.* **2017**, *29*, 10299−10311.
(47) Yi, L.; Liu, Z.; Yu, R.; Zhao, C.; Peng, H.; Liu, M.; Wu, B.; Chen, M.; Wang, X. Li-Rich Layered/Spinel Heterostructured Special Morphology Cathode Material with High Rate Capability for Li-Ion Batteries. *ACS Sustainable Chem. Eng.* **2017**, *5*, 11005−11015.
(48) Bréger, J.; Jiang, M.; Dupré, N.; Meng, Y. S.; Shao-Horn, Y.; Ceder, G.; Grey, C. P. High-resolution X-ray diffraction, DIFFaX, NMR and First Principles Study of Disorder in the Li_2MnO_3-$Li[Ni_{1/2}Mn_{1/2}]O_2$ solid solution. *J. Solid State Chem.* **2005**, *178*, 2575−2585.
(49) Chen, D.; Mahmoud, M. A.; Wang, J.-H.; Waller, G. H.; Zhao, B.; Qu, C.; El-Sayed, M. A.; Liu, M. *Operando* Investigation into Dynamic Evolution of Cathode-Electrolyte Interfaces in a Li-Ion Battery. *Nano Lett.* **2019**, *19*, 2037−2043.
(50) Hong, J.; Seo, D.-H.; Kim, S.-W.; Gwon, H.; Oh, S.-T.; Kang, K. Structural Evolution of Layered $Li_{1.2}Ni_{0.2}Mn_{0.6}O_2$ upon Electrochemical Cycling in a Li Rechargeable Battery. *J. Mater. Chem.* **2010**, *20*, 10179−10186.
(51) Kavas, H.; Baykal, A.; Toprak, M. S.; Köseoğlu, Y.; Sertkol, M.; Aktaş, B. Cation Distribution and Magnetic Properties of Zn Doped $NiFe_2O_4$ Nanoparticles Synthesized by PEG-Assisted Hydrothermal Route. *J. Alloys Compd.* **2009**, *479*, 49−55.
(52) Yabuuchi, N.; Yoshii, K.; Myung, S.-T.; Nakai, I.; Komaba, S. Detailed Studies of a High-Capacity Electrode Material for Rechargeable Batteries, Li_2MnO_3-$LiCo_{1/3}Ni_{1/3}Mn_{1/3}O_2$. *J. Am. Chem. Soc.* **2011**, *133*, 4404−4419.
(53) Naushad, M.; Ahamad, T.; Al-Maswari, B. M.; Abdullah Alqadami, A.; Alshehri, S. M. Nickel Ferrite Bearing Nitrogen-Doped Mesoporous Carbon as Efficient Adsorbent for the Removal of Highly Toxic Metal Ion from Aqueous Medium. *Chem. Eng. J.* **2017**, *330*, 1351−1360.
(54) Moses, A. W.; Flores, H. G. G.; Kim, J.-G.; Langell, M. A. Surface Properties of $LiCoO_2$, $LiNiO_2$ and $LiNi_{1-x}Co_xO_2$. *Appl. Surf. Sci.* **2007**, *253*, 4782−4791.
(55) Cherkashinin, G.; Ensling, D.; Jaegermann, W. $LiMO_2$ (M = Ni, Co) Thin Film Cathode Materials: A Correlation between the Valence State of Transition Metals and the Electrochemical Properties. *J. Mater. Chem. A* **2014**, *2*, 3571−3580.
(56) Sun, B.; Lou, S.; Zheng, W.; Qian, Z.; Cui, C.; Zuo, P.; Du, C.; Xie, J.; Wang, J.; Yin, G. Synergistic Engineering of Defects and Architecture in Co_3O_4@C Nanosheets Toward Li/Na Ion Batteries with Enhanced Pseudocapacitances. *Nano Energy* **2020**, *78*, 105366.
(57) Wu, H.; Yang, T.; Du, Y.; Shen, L.; Ho, G. W. Identification of Facet-Governing Reactivity in Hematite for Oxygen Evolution. *Adv. Mater.* **2018**, *30*, 1804341.
(58) Ding, X.; Luo, D.; Cui, J.; Xie, H.; Ren, Q.; Lin, Z. An Ultra-Long-Life Lithium-Rich $Li_{1.2}Mn_{0.6}Ni_{0.2}O_2$ Cathode by Three-in-One Surface Modification for Lithium-Ion Batteries. *Angew. Chem., Int. Ed.* **2020**, *59*, 7778−7782.
(59) Luo, K.; Roberts, M. R.; Hao, R.; Guerrini, N.; Pickup, D. M.; Liu, Y.-S.; Edström, K.; Guo, J.; Chadwick, A. V.; Duda, L. C.; Bruce, P. G. Charge-Compensation in 3*d*-Transition-Metal-Oxide Intercalation Cathodes Through the Generation of Localized Electron Holes on Oxygen. *Nat. Chem.* **2016**, *8*, 684−691.
(60) Koga, H.; Croguennec, L.; Ménétrier, M.; Mannessiez, P.; Weill, F.; Delmas, C.; Belin, S. *Operando* X-ray Absorption Study of the Redox Processes Involved upon Cycling of the Li-Rich Layered Oxide $Li_{1.20}Mn_{0.54}Co_{0.13}Ni_{0.13}O_2$ in Li Ion Batteries. *J. Phys. Chem. C* **2014**, *118*, 5700−5709.
(61) Koga, H.; Croguennec, L.; Ménétrier, M.; Douhil, K.; Belin, S.; Bourgeois, L.; Suard, E.; Weill, F.; Delmas, C. Reversible Oxygen Participation to the Redox Processes Revealed for $Li_{1.20}Mn_{0.54}Co_{0.13}Ni_{0.13}O_2$. *J. Electrochem. Soc.* **2013**, *160*, A786−A792.
(62) Johnson, C. S.; Li, N.; Lefief, C.; Vaughey, J. T.; Thackeray, M. M. Synthesis, Characterization and Electrochemistry of Lithium Battery Electrodes: $xLi_2MnO_3\cdot(1-x)LiMn_{0.333}Ni_{0.333}Co_{0.333}O_2$ ($0 \le x \le 0.7$). *Chem. Mater.* **2008**, *20*, 6095−6106.
(63) Hy, S.; Felix, F.; Rick, J.; Su, W.-N.; Hwang, B. J. Direct *in Situ* Observation of Li_2O Evolution on Li-Rich High-Capacity Cathode Material, $Li[Ni_xLi_{(1-2x)/3}Mn_{(2-x)/3}]O_2$ ($0 \le x \le 0.5$). *J. Am. Chem. Soc.* **2014**, *136* (3), 999−1007.
(64) Myeong, S.; Cho, W.; Jin, W.; Hwang, J.; Yoon, M.; Yoo, Y.; Nam, G.; Jang, H.; Han, J.-G.; Choi, N.-S.; Kim, M. G.; Cho, J. Understanding Voltage Decay in Lithium-Excess Layered Cathode Materials through Oxygen-Centred Structural Arrangement. *Nat. Commun.* **2018**, *9*, 3285.
(65) Hua, W.; Wang, S.; Knapp, M.; Leake, S. J.; Senyshyn, A.; Richter, C.; Yavuz, M.; Binder, J. R.; Grey, C. P.; Ehrenberg, H.; Indris, S.; Schwarz, B. Structural Insights into the Formation and Voltage Degradation of Lithium- and Manganese-Rich Layered Oxides. *Nat. Commun.* **2019**, *10*, 5365.
(66) Javed, M. S.; Zhang, C.; Chen, L.; Xi, Y.; Hu, C. Hierarchical Mesoporous $NiFe_2O_4$ Nanocone Forest Directly Growing on Carbon Textile for High Performance Flexible Supercapacitors. *J. Mater. Chem. A* **2016**, *4*, 8851−8859.
(67) Cao, W.; Zhang, J.; Li, H. Batteries with High Theoretical Energy Densities. *Energy Storage Materials* **2020**, *26*, 46−55.
(68) Berg, E. J.; Villevieille, C.; Streich, D.; Trabesinger, S.; Novák, P. Rechargeable Batteries: Grasping for the Limits of Chemistry. *J. Electrochem. Soc.* **2015**, *162*, A2468−A2475.
(69) Assat, G.; Iadecola, A.; Foix, D.; Dedryvère, R.; Tarascon, J.-M. Direct Quantification of Anionic Redox over Long Cycling of Li-Rich NMC *via* Hard X-ray Photoemission Spectroscopy. *ACS Energy Lett.* **2018**, *3*, 2721−2728.

https://doi.org/10.1021/acsnano.1c02023
ACS Nano 2021, 15, 11607−11618

(70) Su, Y.; Yuan, F.; Chen, L.; Lu, Y.; Dong, J.; Fang, Y.; Chen, S.; Wu, F. Enhanced High-Temperature Performance of Li-Rich Layered Oxide *via* Surface Heterophase Coating. *J. Energy Chem.* **2020**, *51*, 39−47.
(71) Xu, J.; Sun, M.; Qiao, R.; Renfrew, S. E.; Ma, L.; Wu, T.; Hwang, S.; Nordlund, D.; Su, D.; Amine, K.; Lu, J.; McCloskey, B. D.; Yang, W.; Tong, W. Elucidating Anionic Oxygen Activity in Lithium-Rich Layered Oxides. *Nat. Commun.* **2018**, *9* (1), 947.
(72) Mao, C.; Ruther, R. E.; Geng, L.; Li, Z.; Leonard, D. N.; Meyer, H. M.; Sacci, R. L.; Wood, D. L. Evaluation of Gas Formation and Consumption Driven by Crossover Effect in High-Voltage Lithium-Ion Batteries with Ni-Rich NMC Cathodes. *ACS Appl. Mater. Interfaces* **2019**, *11*, 43235−43243.
(73) Rowden, B.; Garcia-Araez, N. A review of Gas Evolution in Lithium Ion Batteries. *Energy Reports* **2020**, *6*, 10−18.
(74) Foix, D.; Sathiya, M.; McCalla, E.; Tarascon, J.-M.; Gonbeau, D. X-ray Photoemission Spectroscopy Study of Cationic and Anionic Redox Processes in High-Capacity Li-Ion Battery Layered-Oxide Electrodes. *J. Phys. Chem. C* **2016**, *120*, 862−874.
(75) Dedryvère, R.; Laruelle, S.; Grugeon, S.; Gireaud, L.; Tarascon, J. M.; Gonbeau, D. XPS Identification of the Organic and Inorganic Components of the Electrode/Electrolyte Interface Formed on a Metallic Cathode. *J. Electrochem. Soc.* **2005**, *152*, A689−A696.
(76) Aurbach, D. Review of Selected Electrode-Solution Interactions which Determine the Performance of Li and Li Ion Batteries. *J. Power Sources* **2000**, *89*, 206−218.
(77) Malmgren, S.; Ciosek, K.; Hahlin, M.; Gustafsson, T.; Gorgoi, M.; Rensmo, H.; Edström, K. Comparing Anode and Cathode Electrode/Electrolyte Interface Composition and Morphology using Soft and Hard X-ray Photoelectron Spectroscopy. *Electrochim. Acta* **2013**, *97*, 23−32.
(78) House, R. A.; Marie, J.-J.; Pérez-Osorio, M. A.; Rees, G. J.; Boivin, E.; Bruce, P. G. The role of O_2 in O-redox cathodes for Li-ion batteries. *Nat. Energy* **2021**, DOI: 10.1038/s41560-021-00780-2.
(79) Hong, J.; Gent, W. E.; Xiao, P.; Lim, K.; Seo, D.-H.; Wu, J.; Csernica, P. M.; Takacs, C. J.; Nordlund, D.; Sun, C.-J.; Stone, K. H.; Passarello, D.; Yang, W.; Prendergast, D.; Ceder, G.; Toney, M. F.; Chueh, W. C. Metal-Oxygen Decoordination Stabilizes Anion Redox in Li-Rich Oxides. *Nat. Mater.* **2019**, *18*, 256−265.
(80) Inaba, M.; Iriyama, Y.; Ogumi, Z.; Todzuka, Y.; Tasaka, A. Raman Study of Layered Rock-Salt $LiCoO_2$ and its Electrochemical Lithium Deintercalation. *J. Raman Spectrosc.* **1997**, *28*, 613−617.
(81) Flores, E.; Vonrüti, N.; Novák, P.; Aschauer, U.; Berg, E. J. Elucidation of $LixNi_{0.8}Co_{0.15}Al_{0.05}O_2$ Redox Chemistry by *Operando* Raman Spectroscopy. *Chem. Mater.* **2018**, *30*, 4694−4703.
(82) Flores, E.; Novák, P.; Aschauer, U.; Berg, E. J. Cation Ordering and Redox Chemistry of Layered Ni-Rich $LixNi_{1-2y}Co_yMn_yO_2$: An *Operando* Raman Spectroscopy Study. *Chem. Mater.* **2020**, *32*, 186−194.
(83) Singh, G.; West, W. C.; Soler, J.; Katiyar, R. S. *in Situ* Raman spectroscopy of layered solid solution Li_2MnO_3-$LiMO_2$ (M = Ni, Mn, Co). *J. Power Sources* **2012**, *218*, 34−38.
(84) Seo, D.-H.; Lee, J.; Urban, A.; Malik, R.; Kang, S.; Ceder, G. The Structural and Chemical Origin of the Oxygen Redox Activity in Layered and Cation-Disordered Li-Excess Cathode Materials. *Nat. Chem.* **2016**, *8*, 692−697.
(85) Li, X.; Qiao, Y.; Guo, S.; Xu, Z.; Zhu, H.; Zhang, X.; Yuan, Y.; He, P.; Ishida, M.; Zhou, H. Direct Visualization of the Reversible O^{2-}/O^{-} Redox Process in Li-Rich Cathode Materials. *Adv. Mater.* **2018**, *30*, 1705197.
(86) Sathiya, M.; Rousse, G.; Ramesha, K.; Laisa, C. P.; Vezin, H.; Sougrati, M. T.; Doublet, M. L.; Foix, D.; Gonbeau, D.; Walker, W.; Prakash, A. S.; Ben Hassine, M.; Dupont, L.; Tarascon, J. M. Reversible Anionic Redox Chemistry in High-Capacity Layered-Oxide Electrodes. *Nat. Mater.* **2013**, *12*, 827−835.
(87) Gent, W. E.; Lim, K.; Liang, Y.; Li, Q.; Barnes, T.; Ahn, S.-J.; Stone, K. H.; McIntire, M.; Hong, J.; Song, J. H.; Li, Y.; Mehta, A.; Ermon, S.; Tyliszczak, T.; Kilcoyne, D.; Vine, D.; Park, J.-H.; Doo, S.-K.; Toney, M. F.; Yang, W.; Prendergast, D.; Chueh, W. C. Coupling between Oxygen Redox and Cation Migration Explains Unusual Electrochemistry in Lithium-Rich Layered Oxides. *Nat. Commun.* **2017**, *8*, 2091.
(88) Ben Yahia, M.; Vergnet, J.; Saubanère, M.; Doublet, M.-L. Unified Picture of Anionic Redox in Li/Na-ion batteries. *Nat. Mater.* **2019**, *18*, 496−502.
(89) Chen, Q.; Pei, Y.; Chen, H.; Song, Y.; Zhen, L.; Xu, C.-Y.; Xiao, P.; Henkelman, G. Highly Reversible Oxygen Redox in Layered Compounds Enabled by Surface Polyanions. *Nat. Commun.* **2020**, *11*, 3411.
(90) Jehnichen, P.; Korte, C. *Operando* Raman Spectroscopy Measurements of a High-Voltage Cathode Material for Lithium-Ion Batteries. *Anal. Chem.* **2019**, *91*, 8054−8061.
(91) Wu, Z.-L.; Xie, H.; Li, Y.; Zhang, F.; Wang, Z.; Zheng, W.; Yang, M.; Cao, Y.; Lu, Z. Insights into the Chemical and Structural Evolution of Li-Rich Layered Oxide Cathode Materials. *Inorg. Chem. Front.* **2021**, *8*, 127−140.
(92) Mohanty, D.; Li, J.; Abraham, D. P.; Huq, A.; Payzant, E. A.; Wood, D. L.; Daniel, C. Unraveling the Voltage-Fade Mechanism in High-Energy-Density Lithium-Ion Batteries: Origin of the Tetrahedral Cations for Spinel Conversion. *Chem. Mater.* **2014**, *26*, 6272−6280.
(93) Singer, A.; Zhang, M.; Hy, S.; Cela, D.; Fang, C.; Wynn, T. A.; Qiu, B.; Xia, Y.; Liu, Z.; Ulvestad, A.; Hua, N.; Wingert, J.; Liu, H.; Sprung, M.; Zozulya, A. V.; Maxey, E.; Harder, R.; Meng, Y. S.; Shpyrko, O. G. Nucleation of Dislocations and Their Dynamics in Layered Oxide Cathode Materials during Battery Charging. *Nat. Energy* **2018**, *3*, 641−647.

https://doi.org/10.1021/acsnano.1c02023
ACS Nano 2021, 15, 11607−11618